Case History

Improving the interpretability of air-gun seismic reflection data using deterministic filters: A case history from offshore Cape Leeuwin, southwest Australia

Colin Sargent[1], Richard W. Hobbs[1], and Darren R. Gröcke[1]

ABSTRACT

To identify drilling targets for an Integrated Ocean Drilling Program project to investigate high-latitude black shales required reinterpretation of legacy seismic data. The original processing had identified the major structures but was of insufficient resolution to map the more-subtle markers at the top of the shale sequence. By reprocessing these 2004 vintage 2D air-gun marine seismic reflection data we show that the application of filters determined from deepwater data yields subbottom geological imaging superior to statistical methods and arguably better than modeled source deconvolution methods, particularly for recovery of low frequencies. The data were acquired to the southwest of Australia in an area with swells that are typically 2–4 m and cause distortions to the predicted source and receiver response functions. These distortions cannot be incorporated in an idealized modeled source function; hence, we have opted to design the deterministic filters from the seismic data. We applied the deconvolution in two steps: a prestack filter to suppress the air-gun bubble pulse signal and a poststack filter to suppress the notches in the amplitude spectrum caused by the free-surface reflections at the source and the receiver. Through this strategy, we expanded the seismic data bandwidth at the low and high frequencies and improved resolution. The tie with the single borehole in the area was significantly improved and has enabled a more-confident interpretation of the shale horizons.

INTRODUCTION

Deconvolution is a fundamental step in the processing of seismic reflection data, and despite advances in acquisition systems and processing algorithms, it can still be problematic. The function of a deconvolution filter is to improve resolution, and its uses include suppressing short-period multiples, compressing the source function, and compensating for acquisition filters. Deconvolution is also important in the suppression of longer-period multiples, e.g., surface-related multiple elimination (SRME) (Verschuur et al., 1992), which are more robust if the source function is known or the data are preconditioned to compress the source function to a band-limited spike. Modern acquisition systems provide the means to directly estimate the source during the survey (Ziolkowski et al., 1982), which is then used to

design the deconvolution filter, but this technology is not available for the majority of the legacy data that are the focus of this paper. For these data, trace-by-trace statistically derived filters based on Weiner theory are still widely used even though the underlying assumptions are violated. Although developments of other types of filter design and optimization can yield improved resolution, e.g., maximum entropy and time-varying deconvolution (Van der Baan, 2008), here we develop a simple yet robust prestack deconvolution filter strategy specifically targeted to compress the source function. Our prestack filter does not require time-varying compensation or transformation of the data into the τ-p domain to ensure periodicity as it is nondirectional. Then a poststack filter is used to maximize resolution.

The objective of the research is to delineate a thick sequence of Cretaceous black shale in preparation for a proposal to the

Integrated Ocean Drilling Program (IODP) to investigate ocean anoxic events and short glaciation events during a period of elevated global temperatures at high latitudes, where there is the best chance to quantify the stability of the climate (Alley and Frakes, 2003; Bornemann et al., 2008; Fluteau et al., 2007). The single Deep Sea Drilling Project (DSDP) borehole penetrated the shale sequence on the Naturaliste Plateau to the southwest of Australia. The top of the black shale is marked by a series of thin chert layers (Davies et al., 1974), but these were not evident in the original processed seismic data images. Further, there were concerns over the cause of a weak bottom-simulating reflector that may indicate the presence of hydrate. In this paper we use this legacy data to evaluate different processing strategies to compress the source and receiver response functions and expand the bandwidth of the data to improve the resolution and, hence, clarity for interpretation.

A seismogram is the convolution of the acquisition impulse response (including those of source, receiver, and data logger) with the earth's reflectivity plus noise. To recover the earth's reflectivity, inverse filters are used to compensate for the acquisition impulse response. The strategies we compare use different inverse filters that are either deterministic filters derived from the seismic data and from external models of the expected source wavelet or statistically derived filters derived from the seismic data. We introduce the concept of a "notional source function," which is a nondirectional prestack filter specifically designed to compress the wavelet by suppression of the air-gun bubble pulse. Our aim is to find a generic strategy that can be easily applied and is reasonably robust.

When high-pressure air is released in seawater from an air-gun chamber, an air bubble rapidly expands in the seawater, generating an acoustic pulse. The bubble continues to expand beyond the point where the internal gas pressure of the air bubble is equal to the hydrostatic pressure. The net force is now directed inward; the out-

ward motion of the bubble decelerates, comes to rest, and converges, recompressing the air. This implosion starts a new cycle, a process that continues repeatedly until all the energy is dissipated or the rising air bubble breaks the sea surface (e.g., Sheriff and Geldart, 1995). Hence, in an air-gun array, the acoustic output of each individual air gun is a long, damped, oscillatory signal. The general shape of the signal is the same for air guns of different chamber volumes with the amplitude and periodicity related by a scaling law (Ziolkowski et al., 1980). When an array of air guns of different chamber volumes are discharged simultaneously, the interactions are complex, with the signals for any individual air gun being modified by the pressure fields of the other air guns in the array (Ziolkowski et al., 1982). However, the initial peaks superimpose, whereas the oscillatory bubble pulses destructively interfere. This destructive interference is further enhanced by the free-surface reflection or source ghost. The resulting signal is a good approximation of an ideal marine seismic source: a sharp impulse lasting only a few milliseconds. However, complete destructive interference of the bubble pulses is not usually achieved, so the source typically contains a vestige of the oscillatory bubble pulse coda, which, if not suppressed by filtering, can reduce clarity and increase ambiguity in interpretation. In the power spectrum of seismic data the remnant bubble pulse creates a low-frequency peak at its fundamental, typically at 8–10 Hz, with a series of harmonics extending up to at least 30 Hz. The prominent notches in the spectrum, typically above 50 Hz, are created by destructive interference caused by the source ghost and also the receiver ghost. The ghosts also suppress the low frequencies with a notch at zero frequency.

For detailed geological interpretation of the final migrated product it is necessary to expand the signal bandwidth of the seismic data, preferably at the low and high ends of the frequency spectrum. For seismic data acquired with a conventional single source and hydrophone streamer, bandwidth expansion is normally achieved by statistical deconvolution methods or estimates of the far-field source signature based on direct measurement or modeling. Here we compare the different approaches and conclude that deterministic filters offer the best approach to expanding the signal bandwidth and therefore improve the geologic interpretability. Further, we conclude that for these data the deconvolution filters are best estimated from the seismic data rather than idealized models.

LOCATION AND GEOLOGICAL SETTING OF THE STUDY AREA

Offshore adjacent to Cape Leeuwin, southwest Australia, is the Naturaliste Plateau (Figure 1), a submarine feature approximately 90,000 km^2 in areal extent lying between 2500 and 3000 m water depth. The southern and western edges of the plateau are defined by steep scarps facing the Diamantina Zone, whereas the northern and eastern flanks slope gently into the Perth Abyssal Plain (Jongsma and Petkovic, 1977). Sediment thickness over most of the Naturaliste Plateau is less than 800-ms two-way traveltime, increasing only in the small rift basins embedded within the plateau (Borissova, 2002). Due to the sparse data available, the origins of the Naturaliste Plateau are not fully understood. Geophysical seismic and potential field studies (Petkovic, 1975; Jongsma and Petkovic, 1977; Borissova, 2002; Direen et al., 2007) and chemical analysis of dredged material (Halpin et al., 2008) and borehole cores (Ford, 1975) suggest
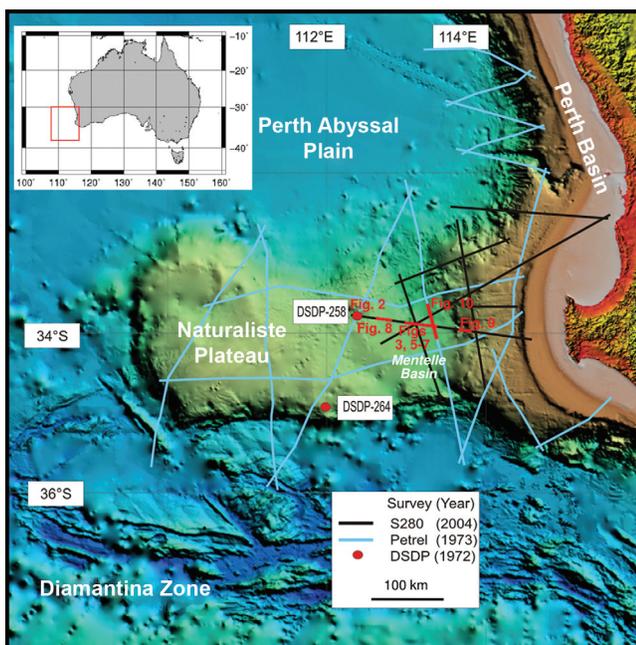

Figure 1. Study area offshore Cape Leeuwin, Australia. Seismic reflection surveys and wells referred to in the text are superimposed on a bathymetric map (modified from Borissova, 2002).

that the Naturaliste Plateau is a lower-crustal extensional alloch-thon sited close to the triple junction that formed during the final stages of Gondwana breakup (Direen et al., 2008). Igneous activity related to the Permo-Cretaceous rifting of greater India and Australia has been interpreted in seismic data from the northern part of the Perth Basin on the West Australian Shelf (Gorter and Deighton, 2002). Westward-orientated small submarine canyons incise the continental slope running into the bathymetric Naturaliste Trough that overlies the geologic Mentelle Basin. At least 3000-ms two-way traveltime of sediments is observed at its main depocenter, and sediments range in age from Cretaceous to Holocene. The sequence has been drilled once by borehole DSDP-258 (Figure 1). The well log reports a thick black shale sequence at depths of 285–514 m below the seafloor. Below the shale, the drill penetrated a further 11 m into a glauconitic sandstone. Above the shale (114–285 m) is a chalk with thin layers of chert. The upper post unit (0–114 m) is carbonate ooze (Davies et al., 1974) (Figure 2). These sediments thin to the west and onlap onto the shallow basement of the Naturaliste Plateau. To the east, the Perth Basin contains several commercial hydrocarbon fields (Iasky, 1993; Mory and Iasky, 1996). The location of the survey area (Figure 1) is exposed to the westerlies, which over the fetch of the southern Indian Ocean, build significant swells that are typically 2 m or more.
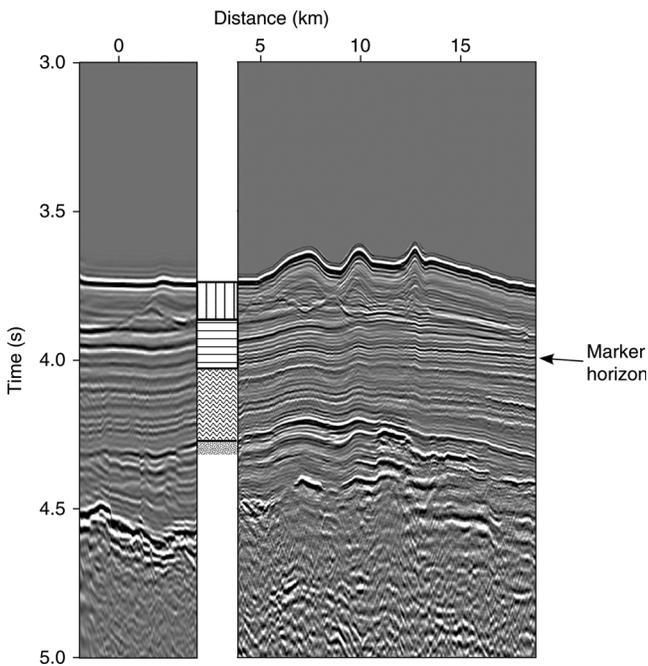

Figure 2. DSDP-258 interpreted lithology tied to the S280-501 seismic profile. The vertical hatching is 114 m of Miocene deep-water carbonate oozes and pelagic sedimentation; the diagonal hatching is 171 m of Paleogene limestones and chalks with occasional chert bands; the wavy hatching is 229 m of Cretaceous black shale; the stippled area represents the bottom 11 m of the borehole, which penetrated into a Lower Cretaceous sequence of glauconitic sands. The seismic section to the left of the borehole has the original processing. The section to the right is the result of the reprocessing described in this paper. Of particular note is the reflection doublet at about 4 s, which was not resolved in the original processing and is used as a basin-wide marker horizon that is ~20 m above the weakly reflective top shale.

DATA PROCESSING

Our principal target is the stratigraphy of the Mentelle Basin over the two-way traveltime interval of 4–6.5 s. This means that we are not troubled by the free-surface multiple but our resolution is compromised by remnant energy in the source bubble pulse coda and the source and receiver ghosts. In the following, we describe our deterministic strategy for the removal of the source bubble pulse coda and ghost notches. We then compare our results with those obtained using filters derived statistically and from a modeled source wavelet and with the original commercial processing.

The raw shot records for the 2D S280 seismic reflection survey were provided by Geoscience Australia. The survey was acquired in 2004 with a 80.3-l (4900 cu in) air-gun array and a 480-channel digital recording streamer with a group length of 12.5 m, yielding profiles with a 6.25-m common midpoint (CMP) spacing (full specifications are given in Table 1). The objective was to maximize the temporal resolution of the deep-water thick Mentelle Basin Cretaceous sequence and tie the geological interpretation to borehole DSDP-258 (Davies et al., 1974) (Figures 1 and 2).

Geometry was applied to the shot and receiver locations and time shifted to the sea-surface reference datum to compensate for the tow depths of the source and receiver. Figure 3a shows an expanded section of an initial brute stack. Geological horizons are observed pinching out at the seabed. Crosscutting these horizons is

Table 1. Acquisition specifications for the Geoscience Australia S280 survey.

| Parameter	Value
Seismic source array	
Source type	Tuned point-source air-gun array
Gun type	Bolt 1500LL and 1900LL-XT air guns
Nominal source volume	80.3 L (4900 cu in)
Nominal source pressure	13.4 MPa (1950 psi)
Nominal source depth	8 ± 1 m
Shotpoint interval	37.5 m
Hydrophone streamer array	
Streamer type	Syntrak 960-24 RDA digital
Number	1
Length	6000 m
Number of groups	480
Group length	12.5 m
Nominal streamer depth	12 ± 1 m
Nominal inline offset	134 m
Data recording system	
Recording system	Syntrak 960-24 MSRS
Record length	12 s
Sample interval	2 ms
Low-cut filter/slope	Out
High-cut filter/slope	206 Hz at 276 dB/octave
Recording format	SEG-D 8058, Rev-1

a broad, diffuse event running approximately 120 ms subparallel below the seabed reflection, which is caused by the source bubble pulse. The possibility of this event being a bottom-simulating reflector caused by hydrate formation is discounted because no reports of hydrates were made in the DSDP-258 borehole and the period and amplitude of the event are consistent with source wavelet models (Figure 4a). The inset in Figure 3a shows the average normalized autocorrelation function for a near-offset record for two time windows, one including the seafloor and the other the top of acoustic basement; both show the same peak in the autocorrelation at a 120-ms lag, which confirms this interpretation. In the frequency domain the source bubble pulse appears as a series of

spikes at low frequencies, modulating the overall shape of the amplitude spectrum (Figure 3b).

Deterministic filters

By their nature, deterministic inverse filters have to be precise; otherwise, they will distort the data by wrongly emphasizing some frequencies in the data at the expense of others and may render the whole data set uninterpretable. So this type of filter can be considered as high risk, but when they work, the benefits to interpretation can be significant, so as such, they can also be high gain. In the raw shot gather domain, the recorded wavelet from a

Figure 3. (a) Portion of an S280 profile brute stack over the eastern margin of the Mentelle Basin. Below the seabed reflection is a sequence of sedimentary units separated by unconformities at about 4.3, 4.5, and 5.2 s measured below the surface location at 85 km. The lowermost unit lies over the acoustic basement (6.0 s), which is interpreted as the pre-Gondwana breakup surface. The inset shows the average autocorrelation functions for a near-offset trace from the prestack shot gathers for the two 1-s windows marked: window 1 encompasses the seabed, and window 2 encompasses the top of the acoustic basement. Both show a peak at 120-ms lag that is caused by the source bubble pulse. This energy can also be seen in the brute stack as a blurred seabed following reflection with a delay of about 120 ms. (All subsequent autocorrelation functions use the same design windows.) (b) Power spectrum that shows the influences of the source and receiver ghost notches at 94 and 64 Hz, respectively, and the fundamental and harmonics of the bubble pulse coda of the source wavelet at 8, 16, 24, and 32 Hz. (All power spectra in this paper are the average computed from the data shown in the corresponding t-x section).
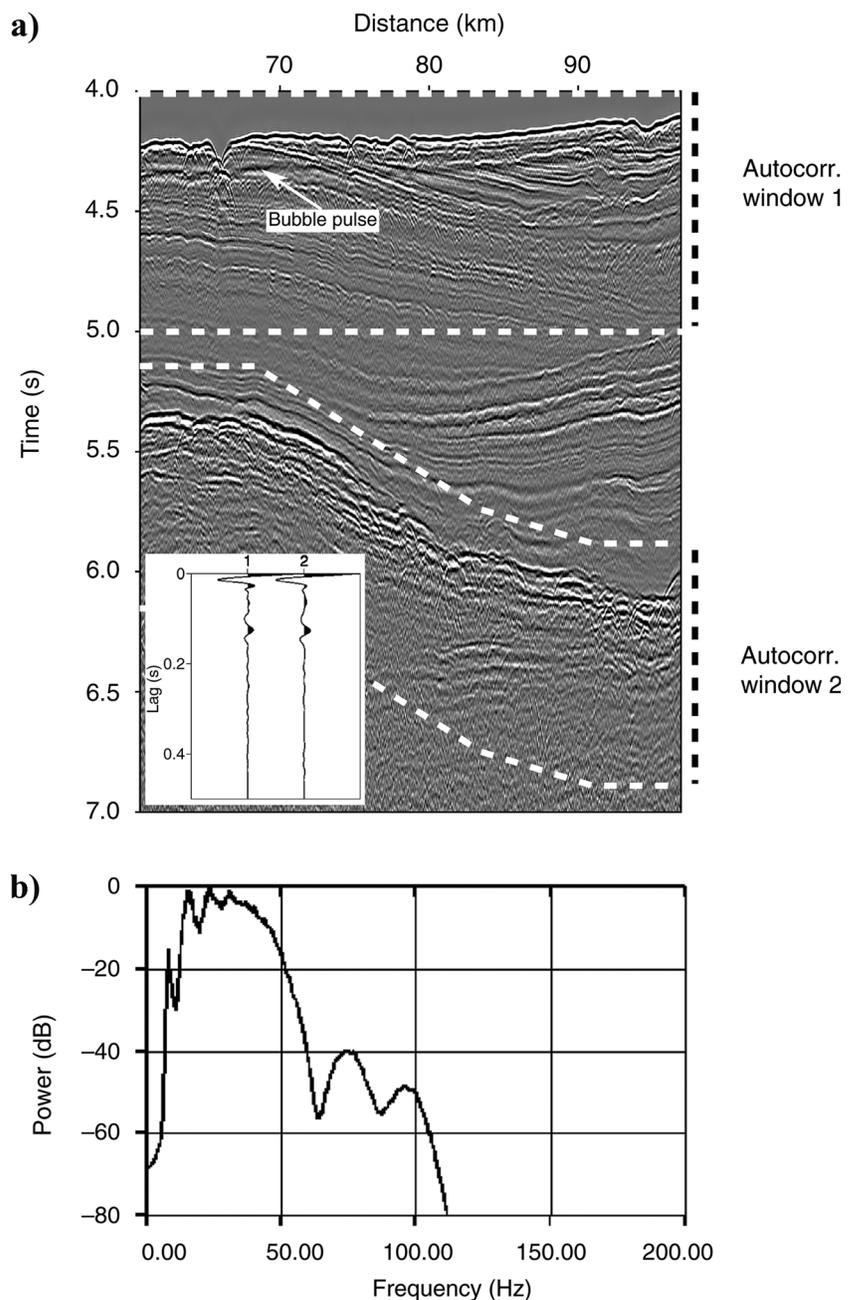
reflection is dependent on the notional source function (which we define hereafter as the far-field acoustic output of the air-gun array at the ambient hydrostatic pressure but without the free-surface ghost) and on the source and receiver ghosts whose periodicity depends on the angle of the raypath at the source and the receiver. Normally, the notional source function and source ghost are considered together and called the far-field source wavelet.

The air-gun array wavelet can be monitored during acquisition, and the required angle-dependent far-field source wavelet can be constructed from the summation of the notional sources derived for each of the individual air guns (Ziolkowski et al., 1982) or from the far-field wavelet recorded directly or derived from a calibrated reference source (Hobbs and Jakubowicz, 2000). However, in general, the source signature is not known. So there are two choices to obtain an estimate of the far-field source wavelet, either using a calibrated source modeling code or estimating directly from the data.

Here we use the Nucleus® source modeling package supplied by Petroleum Geo-Services (PGS). By defining the geometry of the array, the type and volume of each gun, operating air pressure, and details of the data logger instrument filters and sound speed in the water, an angular-dependent estimate of the far-field source wavelet is calculated (Figure 4a). The model assumes that the sea surface is flat, which is not strictly valid, especially for this survey with swells of 2–3 m. The far-field source wavelet and the receiver ghost are sensitive to the sea surface as it continually changes the geometry (Laws and Kragh, 2000). To predict and suppress the source and receiver responses prestack would require them to be modeled shot by shot, hydrophone by hydrophone with a time dependency (Kragh et al., 2004). The alternative strategy is to estimate the source directly from the data. The rationale is that this will also compensate for the variability in the recorded wavelet

caused by the swell. However, with any data-derived filter there is a trade-off in recovering the source wavelet and excluding information about the earth's reflectivity. In the following we develop and demonstrate a robust strategy where we determine deconvolution filters from the seismic data that effectively suppress the remnant source bubble pulse and the ghosts.

The processing methodology is summarized in Table 2 (processing route 1). First, the S280 raw shot records are preconditioned with a simple time-invariant minimum-phase Butterworth band-pass filter to remove low-frequency swell noise. The strategy to suppress the effects of the source bubble and the ghost notches proceeds in two steps and produces two deterministic filters. The first, the debubble filter, is applied prestack to suppress only the bubble pulse coda, and the second, the deghost filter, is applied poststack and suppresses the ghost notches. The rationale for this approach is that the periodicity of the bubble pulse is quite stable from shot to shot because the tow depth, and hence the hydrostatic pressure, is well controlled. After stacking the traces in each CMP gather, the variability in the free-surface ghost reflections is averaged. Poststack, we suppress the ghost notches using a single filter that corresponds to this average. This is shown to work effectively provided that constant mean depths of the source and receiver are maintained.

To estimate the debubble filter, we select a near-offset trace from a number of shot records. The selection criteria are as follows: the selected offset needs to be as free as possible from noise contamination from the towing ship yet close to normal incidence to minimize the angular dependence of the free-surface ghost reflections on traveltime; also, the total number of shots needs to ensure that there is sufficient variation in geological structure so the averaged power spectrum of the data is dominated by effects of the seismic source and free-surface
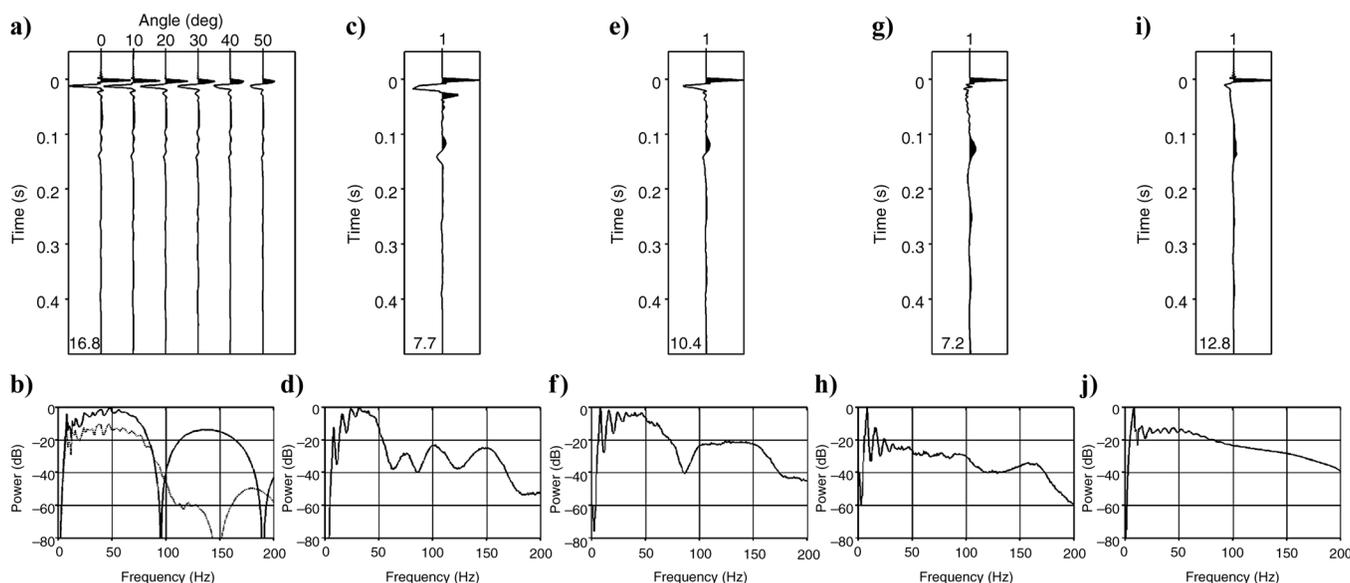

Figure 4. The modeled and estimated far-field source wavelets and their power spectra. Where present, the number to the left of the trace is its peak-to-bubble ratio. (a) The source wavelet (including source ghost) as modeled by the Nucleus software (six angles of incidence are plotted from 0° to 50°) and (b) the spectra for the 0° and 50° wavelets. The source ghost notch moves from 94 to 145 Hz, whereas the low-frequency peaks from the source bubble do not change. (c) Estimate of the normal incidence (0°) wavelet derived from the seismic reflection data and (d) its spectrum (note the stronger low-frequency peaks associated with the source bubble). (e) The estimated source function and (f) its spectrum computed from (c) with compensation for the receiver ghost. (g) The notional source function and (h) its spectrum computed from (e) with compensation for the source ghost. (i) The equivalent notional source function and (j) its spectrum computed from Nucleus software.

Table 2. Five alternative processing routes with results displayed in Figure 7. Routes 1–4 have been developed and tested as part of this work; route 5 is the original processing done for Geoscience Australia; DBS is deconvolution before stack, and DAS is deconvolution after stack. Because the objective was to evaluate alternative prestack and poststack deconvolution filters, wherever possible, all other processing stages are common; NA indicates where a processing stage is not applicable.

Processing routes				
1	2	3	4	5
Deterministic data derived DBS and DAS	Deterministic model derived DBS data derived DAS	Combined model derived DBS statistical DAS	Statistical DBS and DAS	Original processing statistical DBS
Reformat and assign geometry −6.25-m CMP interval				(3.125m CMP interval)
NA	NA	NA	NA	Despiking
NA	NA	NA	NA	Divergence correction
NA	NA	NA	NA	Linear noise removal
Band-pass filter: Butterworth minimum phase low-cut: 5 Hz/48 dB/oct slope high-cut: 200 Hz/24 dB/oct slope				Band-pass filter: Butterworth minimum phase low-cut: 4 Hz 18 dB/oct slope high-cut: 110 Hz 72 dB/oct slope
NA	NA	NA	Apply $t^{1.5}$ gain	Resample: 4ms
NA	NA	τ-p transform		
Debubble inverse filter to produce a zero-phase band-limited Ormsby wavelet (2-5-80-160 Hz) derived from amplitude spectrum of ghost-free far-field source wavelet extracted from the near offset traces assuming minimum phase	Debubble inverse filter to produce a zero-phase band-limited Ormsby wavelet (2-5-80-160 Hz) derived from amplitude spectrum of ghost-free far-field source wavelet computed from source specifications using Nucleus	Slowness dependent inverse filter to produce a zero-phase band-limited Ormsby wavelet (2-5-80-160 Hz) derived from amplitude spectrum of ghosted far-field source wavelet computed from source specifications using Nucleus	Deconvolution before stack: statistically derived predictive deconvolution filter: gap: 80 ms length: 140 ms design gate: 4 s from seabed +120 ms	Deconvolution before stack: statistically derived predictive deconvolution filter: gap: 48 ms length: 240 ms for shots where the seabed is less than 300 m
NA	NA	t-x transform		
NA	NA	NA	Remove $t^{1.5}$ gain	Rebin to 12.5 m CMP interval
Combined radon domain and Eigen filter long period multiple suppression				Radon multiple suppression
Common offset f-k DMO				Two passes of prestack time migration with velocity picking every 1 km
NMO (picked every 1 km) Outer and inner mute Stack				
NA	NA	Apply t^2 gain		NA
Deghost inverse filter to produce a zero-phase band-limited Ormsby wavelet (2-5-80-160 Hz) derived from amplitude spectrum of stacked data assuming minimum phase		Deconvolution. after stack: statistically derived spiking deconvolution filter: gap: 2 ms; length: 80 ms design gate: 4 s from seabed-100 ms		NA
NA	NA	Remove t^2 gain		NA
Time variant zero-phase Ormsby band-pass filter 0-10-110-150 Hz at seabed (sb) 0-10-110-150 Hz at sb + 0.4 s 10-20-40-60 Hz at sb + 3 s 10-20-30-50 Hz at sb + 3.5 s				NA
f-x deconvolution Time variant gain				
Kirchhoff time migration				NA
Q-compensation $Q = 150$ Cosmetic mute to seabed				
Resample: 4 ms				NA

ghosts. Here we used the data trace from the nearest offset receiver group and 1000 shot records. First-order source and recording streamer ghost notches deeply incise the summed near-channel power spectrum (Figure 4d). Using this spectrum, we computed an equivalent minimum-phase wavelet that we believe to be a fair estimate of the notional source function including the source and receiver ghosts (Hargreaves, 1992). The periods of the ghosts are determined from the notches in the power spectrum. We then applied two simple filters, one for each of the source and receiver ghosts, computed as the inverse of a time series of the form $(1, 0, 0,\ldots, r_{-n},\ldots, r_{-1}, r_0, r_1,\ldots, r_n)$, where the delay of r_0 is set as the period of the source or receiver ghost and the amplitude of $r_{-n},\ldots, r_n$ is a Gaussian distributed function of negative reflection coefficients. This approximation includes compensation for sea-surface shape and source and receiver geometries, which are not explicitly determined. The value of n and the coefficients $r_{-n},\ldots, r_n$ are found by trial and error until the notches in the spectrum are suppressed (Figure 4f and 4h). The optimum strategy is to first assume an ideal reflection coefficient by setting $n = 0$ and $r_0 = -1.0$, then incrementally increase n and modify the coefficients $r_{-n},\ldots,r_n$ accordingly until an acceptable match to the observed notches is found by applying the filters to the previously computed minimum-phase wavelet. After this compensation, the resultant wavelet is then inverted to give the required debubble filter that reduces the notional source function to a zero-phase band-limited response. In this case the limiting frequency range is defined by corner points 2, 5, 80, and 160 Hz. White noise of 1% is added to stabilize the calculation of the filter.

Our processing methodology is shown in Table 2 (option 1). The shot data are filtered using the debubble filter, which is done in the *t-x* domain as it is assumed the filter has no directionality. We believe this assumption is valid because the filter is dominated by the low-frequency bubble pulse, which has a wavelength that is significantly greater than the dimensions of the source and receiver arrays. Any directional errors at higher frequency are carried forward and are compensated in the second deghosting filter. In the example shown, the deepwater environment meant that free-surface multiples did not interfere with the target Cretaceous sediment reflectivity, but on the basin margin the multiples were suppressed using a combined Radon space (Russell et al., 1990) and eigenvector filter (Hardy and Hobbs, 1991). Prestack reflection point smear was reduced by a Fourier domain implementation of dip moveout (DMO) (Hale, 1984). This approach was chosen over more computationally intensive full prestack time migration because the background velocity model was smooth, with the thick Cretaceous sediments having interval velocities of less than 2000 m/s. Prestack DMO is a partial migration that can be combined with poststack migration to yield an equivalent result to full prestack migration (Yilmaz, 2001). After sorting to CMP gathers, the data are stacked with an outer trace mute to avoid normal moveout (NMO) stretch together with an inner trace mute to reduce remnant multiple noise on the basin margins (Figure 5a). The optimum P-wave stacking velocity field was manually picked from velocity analysis panels at 1-km intervals post-DMO.

The debubble process in the shot domain removes the low-frequency remnant air-gun array oscillatory bubble pulses from the data as is evidenced by the inset autocorrelation functions, but it still leaves the power spectrum of the stacked data incised
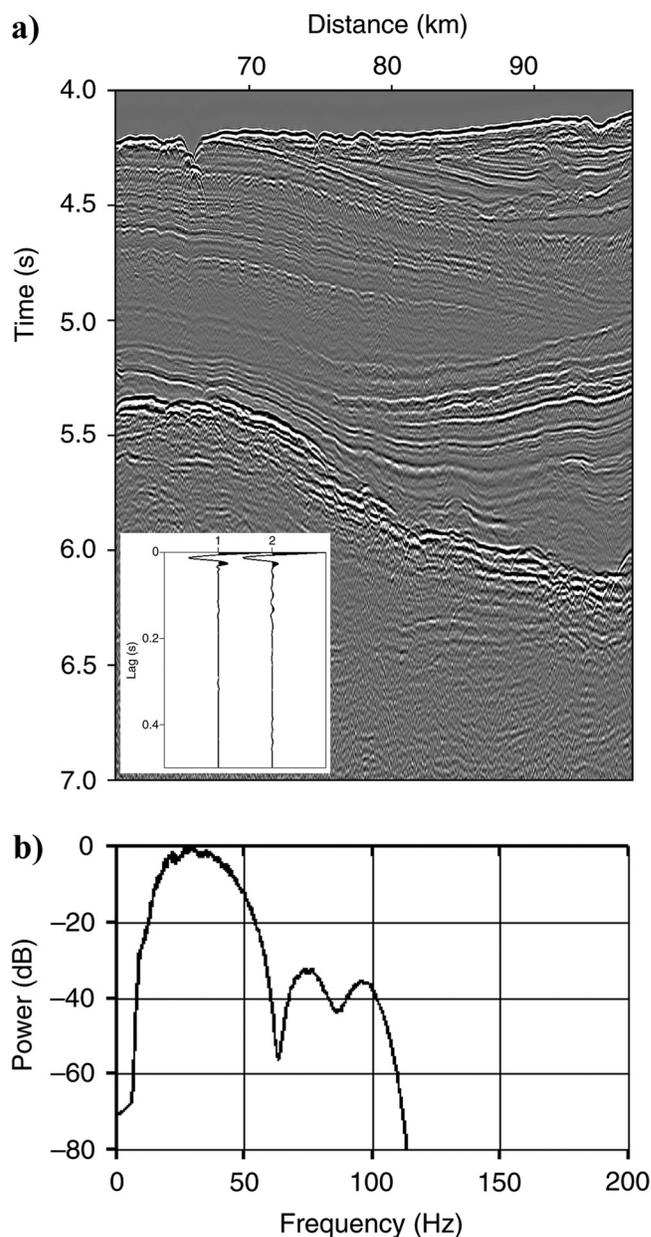

Figure 5. (a) Stack section shown in Figure 2a after application of a source debubble deterministic filter and prestack partial migration (DMO). The inset shows the average autocorrelation functions for a near-offset trace from the prestack shot gathers after application of the prestack debubble filter (design windows as in Figure 3a). (b) Corresponding amplitude spectrum. Note that the low-frequency peaks caused by the source bubble have been suppressed but the source and receiver ghost notches are still present.

by the source and recording streamer ghost notches (Figure 5b). The ghost notches effectively limit the frequency content and, therefore, the temporal resolution of the stacked section. By convolving the poststack data with a designed deghost filter we can address this problem.

The poststack deghost filter is derived in a manner similar to the prestack debubble filter. A section of the stacked data is selected that encompasses a sufficient variation in the geology, in our case 1500 CMP traces, so that the average amplitude

spectrum is dominated by the ghost notches. From the average amplitude spectrum we compute a minimum-phase wavelet that represents the band-limited impulse response of the free-surface ghost reflections convolved with the stack filter. From this we compute a band-limited inverse filter that effectively whitens the spectrum across over the desired frequency range, in our case defined by corner points 2, 5, 80, and 160 Hz. This filter is then convolved with the stacked section (Figure 6).

Poststack time and spatially varying zero-phase band-pass filtering tidied up unwanted spurious low- and high-frequency noise. Amplitude loss was compensated by applying a smooth inverse amplitude decay curve. Poststack Kirchhoff time migration completed the imaging step started with the prestack DMO (Yilmaz, 2001). Frequency-distance (*f-x*) deconvolution (Canales, 1984) was applied prior to time migration to suppress out-of-plane diffractions destroying the continuity of the shallow geology. The out-of-plane diffraction energy is believed to emanate

from a dense 3D polygonal fault system within the thick, fine-grained Cretaceous sedimentary sequence. The processing sequence was completed with a *Q* filter to compensate for anelastic frequency loss and a cosmetic top mute. The final processed section is shown in Figure 7a.

For comparison, the same processing sequence was used, but the deconvolution filters both pre- and poststack were changed to explore the strengths and weaknesses of our proposed processing methodology (see Table 2). To simulate our approach as closely as possible but using an estimate of the notional source function derived from modeling, we substituted the prestack debubble filter with the inverse of the notional source function shown in Figure 4i. This notional source function has been computed assuming a free-surface reflection coefficient of zero. Comparing the spectra of the modeled source (Figure 4j) with the estimated source (Figure 4h) shows that the former is deficient in low frequencies associated with the bubble pulse. As

Figure 6. (a) Stack section shown in Figure 4a after application of the deghost deterministic filter. The inset shows the average autocorrelation functions for the stack traces after application of the poststack deghost filter (design windows as in Figure 3a). (b) Corresponding amplitude spectrum. Now the source and receiver ghost notches are suppressed, although there is still residual high-frequency loss due to absorption and scattering (*Q*). The numbered targets identify the zones used for the comparison of the different processing routes listed in Table 2 and shown in Figure 7.
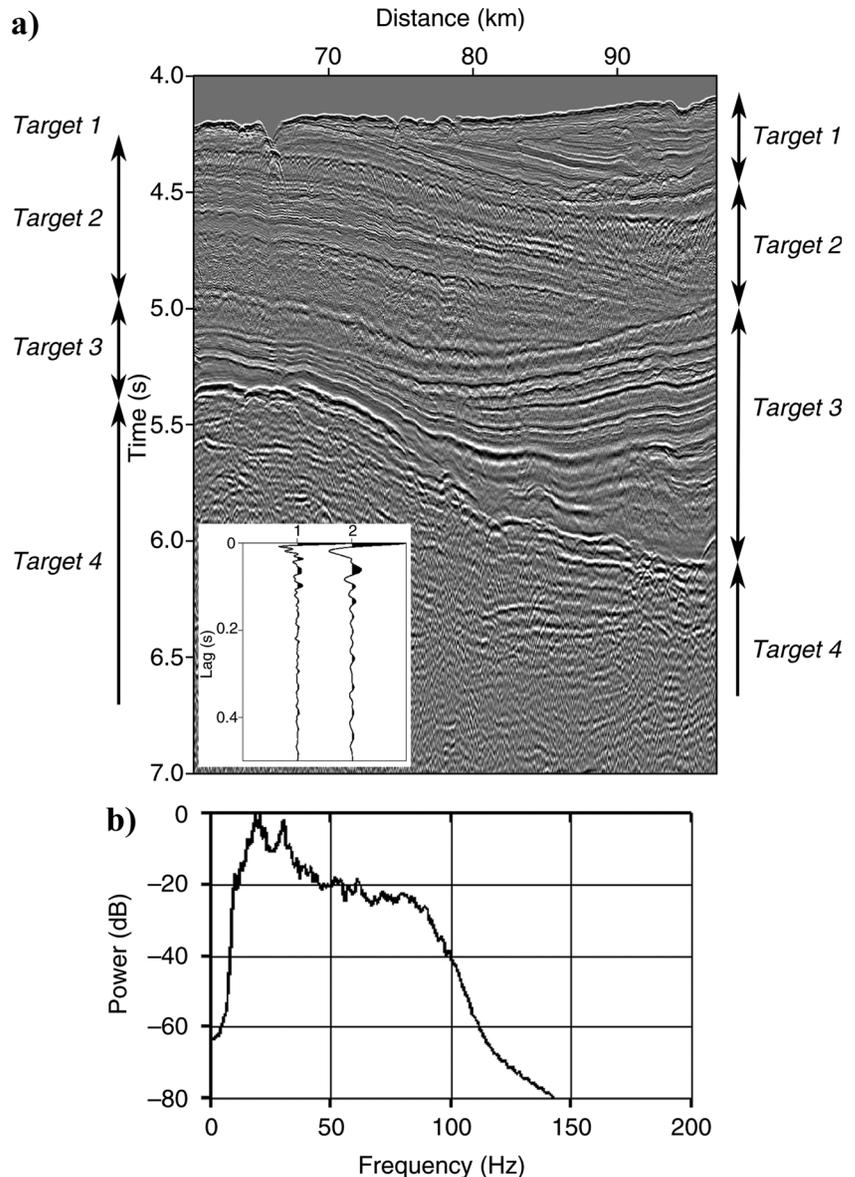
before, this filter is assumed to have no directionality and is applied in the *t-x* domain. The rest of the processing flow was as above, including the design and application of the poststack deghost filter, but this also had to compensate for residual bubble energy not suppressed prestack (Table 2, option 2). The result is shown in Figure 7b. The inset shows the average autocorrelation functions for the time window that includes the seabed (Figure 3a): trace 1 is from a near-offset trace after prestack deconvolution; trace 2 is the stacked trace after poststack deconvolution. A comparison with the same functions using our

derived notional source function (inset in Figure 7a) shows that the modeled source has failed to suppress the bubble pulse, but this has been compensated by the poststack deconvolution filter.

Our third strategy tested a hybrid approach (Table 2, option 3). Here we used a set of angle-dependent filters based on the far-field source wavelets (Figure 4a). These were applied in the τ-p domain and hence necessitated the additional transform back into the *t-x* domain for subsequent processing. This should simultaneously compensate for the source bubble and the source ghost. However, as mentioned above, the modeled source does
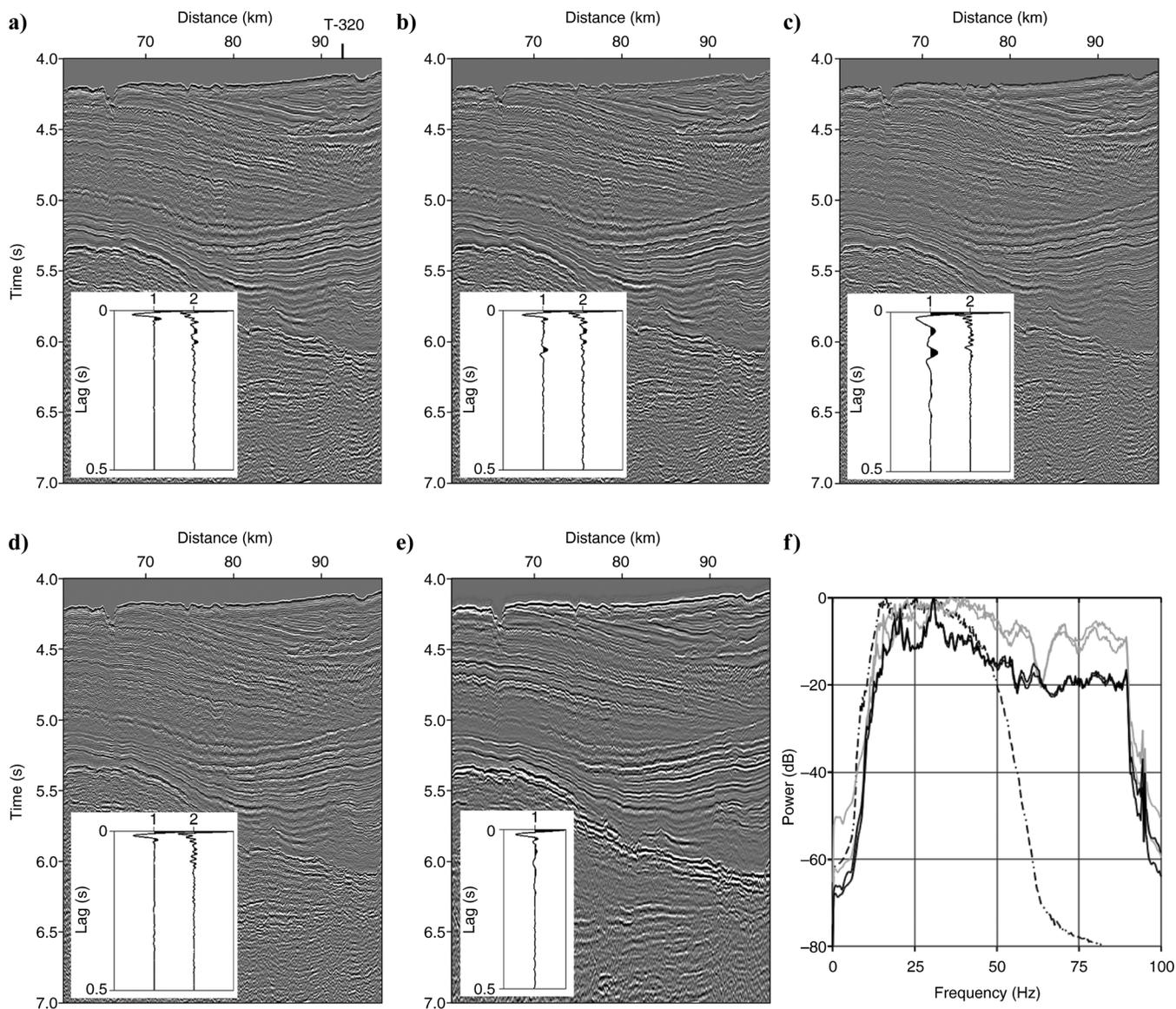

Figure 7. A comparison of the example data panel through the five processing routes shown in Table 2. Insets show the mean autocorrelation function for the first design window (Figure 3a) encompassing the seabed: trace 1 is from a near-offset prestack trace after application of the prestack deconvolution filter; trace 2 is for the stack traces after application of the poststack deconvolution filter. (a) Prestack debubble and poststack deghost filters, (b) prestack filter based on the Nucleus wavelet (Figure 4i) and poststack deghost, (c) prestack filters based on the Nucleus far-field wavelets (Figure 4a) and Wiener-Levinson spiking filter poststack, (d) prestack Wiener-Levinson predictive deconvolution and Weiner-Levinson spiking filter poststack, and (e) original processing with only a Wiener-Levinson predictive deconvolution filter applied prestack. (f) Corresponding power spectra, which fall into three groups. The first pair (black solid lines) result from the deterministic approach (a and b), the second pair (gray solid lines) have a poststack Wiener-Levinson deconvolution (c and d), and the third (dashed-dotted line) is from the original processing (e).

not fully account for the amplitude of the bubble pulse, and the simple sea-surface reflection used in the Nucleus package overestimates the source ghost, so the poststack filter has to compensate for these effects and the residual receiver ghost. Thus, we opted to replace the poststack deghost filter with a Wiener-Levinson minimum-phase statistically derived spiking deconvolution operator that was 80 ms long. The result is shown in Figure 7c.

The last test was to replace pre- and poststack deconvolution filters with statistically derived filters (Table 2, option 4). Prestack, the filter was designed on the autocorrelation of CMP gathers corrected for divergence and transformed into the τ-p domain. The initial wavelet of the source signature was preserved with a prediction lag of 80 ms, whereas the following remnant source bubble pulse was suppressed by a 140-ms operator length. After deconvolution the data were transformed back to the *t-x* domain, and the divergence correction was removed. Poststack, minimum-phase spiking deconvolution with an operator length of 80 ms was used to expand the signal bandwidth again with a divergence gain correction. The result is shown in Figure 7d.

For the original processing (Table 2, option 5) the data processing contractor for Geoscience Australia only applied a prestack predictive deconvolution operator where the seabed traveltime was less than 300 ms with no further bandwidth enhancement

poststack. Also, instead of the DMO/poststack time migration used in our strategy the contractor used two passes of a prestack time migration with an additional revision of the migration velocities. The result is shown in Figure 7e.

Figure 7f shows the power spectra of the final processed sections. Setting aside the original processing, the spectra can be grouped into two distinct responses determined by the poststack deconvolution process applied. The deghost filter produces a generally smooth spectrum (Figure 7f, black solid lines) with some residual low-frequency peaks at the higher harmonics of the bubble pulse frequency for the designed and modeled prestack debubble filters. The Wiener-Levinson filter (Figure 7f, gray solid lines) retains a notch at about 64 Hz that is a small vestige of the original receiver ghost.

DISCUSSION

To compare the differing processing routes, we will consider four targets in the final images. The first target is the seabed and upper sediments down to the channel-cut unconformity at about 4.5 s. The second target is interpreted to be the Cretaceous shale sequence that terminates at a sloping uncomformity that has a maximum traveltime of 5.2 s. The third target is below this uncomformity and includes deeper sediments of unknown age above the top acoustic basement. Finally, the last target is the top acoustic basement and deeper reflectivity (Figure 6).
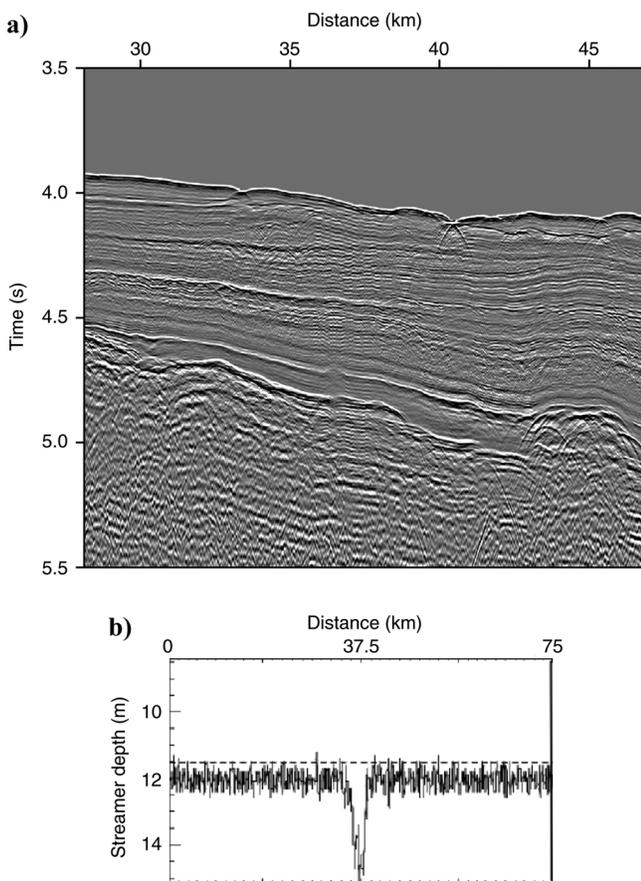

Figure 8. (a) Localized streamer instability induced high-frequency reverberations. (b) Streamer depths along the profile recorded by a depth sensor at approximately 2000-m offset from the quality control data logs. The drop in depth affected the front half of the streamer.
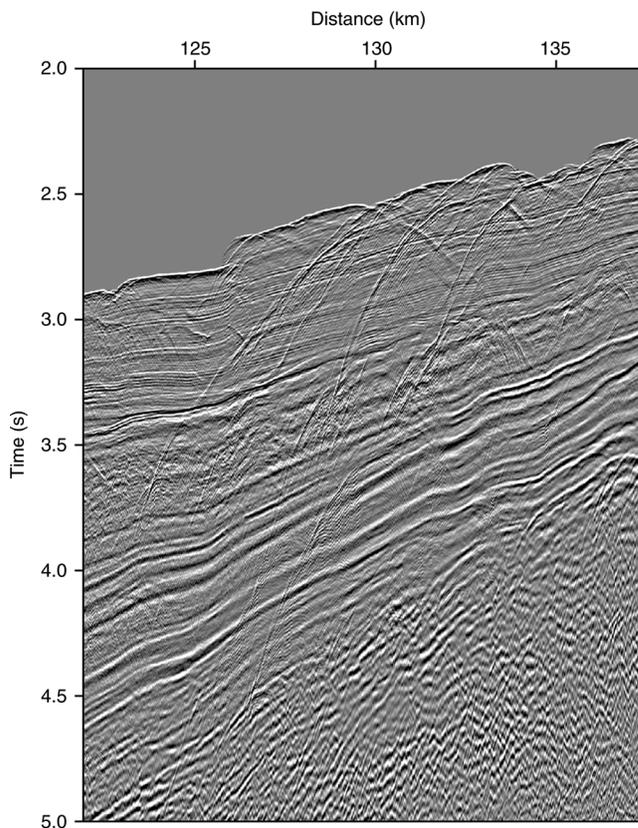

Figure 9. Example of severe sideswipe-induced high-frequency reverberations caused by out-of-plane canyons that are oblique to the seismic profile on the continental margin slope. For location, see Figure 1.
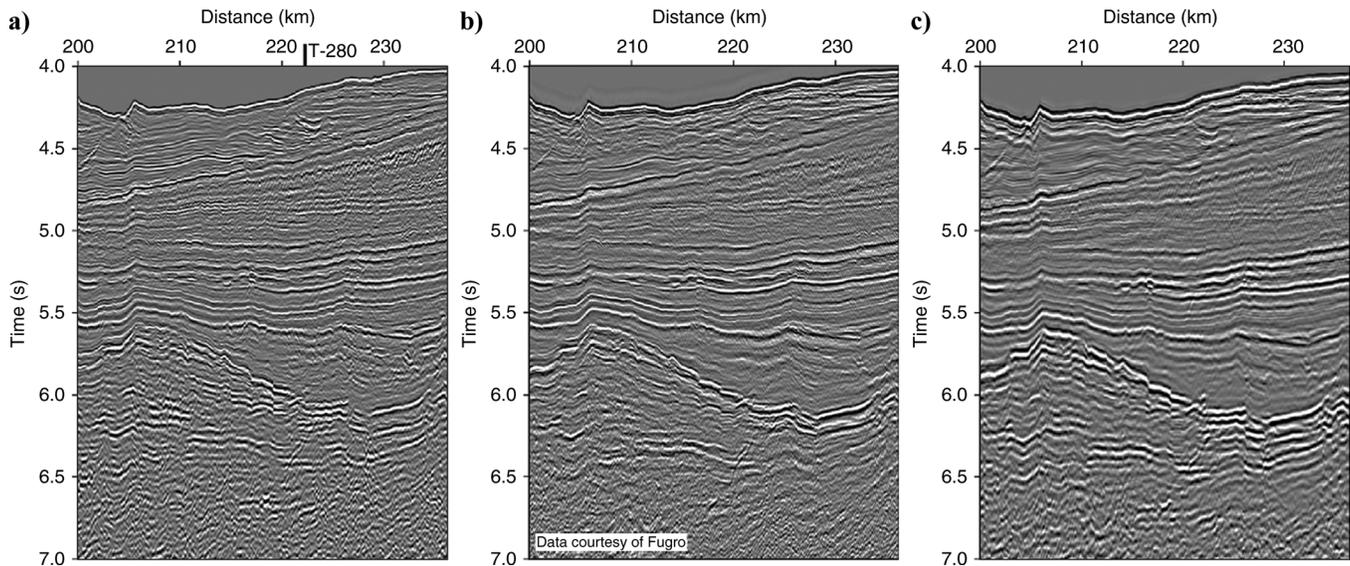
Figure 10. (a) Reprocessed section using our debubble and deghost filters from the Petrel survey where it ties with the S280 profile shown in Figure 7. For location, see Figure 1. (b) An earlier reprocessing of the data. (c) Original processing using a signature deconvolution operator.

Target 1

The seabed is defined in all images, although routes 2 and 3 give the highest resolution. The broader seabed reflection from route 1 is a consequence of the minimum-phase approximation used in the filter design, which is not wholly satisfied at the higher frequencies in the initial acoustic pulse of the air-gun array, whereas these mixed phase components are captured by the Nucleus model. Immediately beneath the seabed, routes 1 and 2 outperform all the other processing options where residual reverberatory noise from the statistical deconvolution filters obscures the shallow unconformity that cuts across the image at around 4.25 s to the right of the seabed canyon. A small phase discrepancy on the channel-cut unconformity (4.5 s, kilometer 85) differentiates the results from routes 1 and 2.

Target 2

Again, routes 1 and 2 outperform routes 3 and 4 in the second target area; the internal structure of the shale sequence is more clearly defined and has less residual reverberations. The original processing (route 5) is also adequate for tracing the major boundaries, but the lower high-frequency filter imposes a severe limit on the interpretation of the finer structures. Again, the phase difference between routes 1 and 2 is apparent, and arguably, the lower-frequency unconformity at the base of this sequence is better defined in route 1.

Target 3

Here the statistical deconvolution (route 4) gives a similar result to that of route 1 in terms of the phase of the reflections. Routes 1 and 2 retain the highest resolution. Route 3 is degraded by high-frequency noise. It is not residual noise created by the transforms into and back out of the τ-p domain because the noise is not present in route 4. An attempt to replace the poststack statistical deconvolution with a deterministic deghost filter as used in routes 1 and 2 (not shown here) did not change the result either, which leads us to the conclusion that the noise has been added by errors in the angular dependence and period of the source ghost during the prestack deconvolution.

Target 4

Routes 1 and 3 result in the sharpest top acoustic basement reflection. Route 4 is also good. Route 2 produced the least clear event, which we believe is due to a persistent phase error, noted earlier, in the low-frequency bubble pulse modeled by the Nucleus software because it cannot model the variability in the notional source function caused by the large swell. The lower-frequency internal reflectivity is best imaged by route 5 (original processing) because the harsher high-cut filter has removed a lot of incoherent noise. However, an overaggressive trace amplitude balance has created a low-amplitude shadow immediately beneath the strong top acoustic basement reflection.

Although routes 1 and 2 arguably produced similar results, the prestack debubble filter based on modeling did not perform well. As shown in Figure 4, the expected modeled source function is significantly different from the one derived from the data in overestimating the peak-to-bubble amplitude ratio. The reasons for this mismatch are not the focus of this paper, but this example serves as a reminder that even well-calibrated modeling codes do not always reproduce the actual source signature. The consequence is that the debubble filter computed from the modeled source fails to suppress the actual bubble pulse in the data (Figure 7b, inset), which may have implications for subsequent prestack processes where it may be used to precondition the data, e.g., SRME. Also, any remnant bubble pulse may confuse velocity analysis in challenging areas like the subbasalt, where because of the low Q (Maresh et al., 2006), the low-frequency bubble may become significant and cause spurious high semblance values, leading to an erroneous velocity model for stacking and migration.

A critical aspect of using deterministic filters is the stability of the acquisition system. We were fortunate that during the

profiling the source was not reconfigured due to air-gun failures. However, we did notice an occasional burst of high-frequency reverberation (Figure 8). Examination of the depth logs of the streamer depth-control birds shows these reverberations are coincident with the temporary loss of streamer control, particularly at the head and middle sections of the streamer. The small change in the tow depth results in a shift in the frequency of the receiver ghost notch. The deterministic filter based on the stable towing state does not fit the compromised streamer, thus introducing noise.

A similar effect is observed in a 2D profile from out-of-plane energy (Figure 9). In this case the "sideswipe" event is generated off the side walls of submarine canyons aligned at right angles to the slope strike that cross the 2D profile at an oblique angle. As the profile diverges from the canyons, the ghost notches in the sideswipe signal deviate from those in the deterministic filter, introducing high-frequency noise into the data. This phenomenon is a diagnostic for sideswipe events that might otherwise be interpreted as geological in origin.

The application of a deterministic deghost filter may not be ideal for shallow-water environments where the design of the filter is compromised because the implicit far-field approximations are no longer valid. The angle of incidence of the near traces, which contribute to the stack, is large, which changes the source far-field signature (Ziolkowski, 1984), and therefore, the frequency of the ghost notches shifted from their ideal location for a normal incidence primary reflection. Normal moveout stretch, even with a severe outside trace mute, and stacking result in the loss of high frequencies; under these conditions, designing a poststack deterministic deghost filter may not be feasible. However, in these situations, if the profile extends into deep water and there are no source configuration changes, then a notional source function derived in the deep water may be used to design a debubble filter that can be successfully applied in the shallow-water section.

The Naturaliste Plateau and Mentelle Basin have been investigated by several seismic reflection surveys, including the 1973 vintage Petrel survey (Figure 1), which used a 17.9-l (1090 cu in) air-gun source firing into a 24-channel digital recording system. Designing and applying source debubble and deghost filters to the Petrel survey data did little to improve the final time migrated section compared to the recent processing using combinations of deterministic and statistically based deconvolution filters (Figure 10). This was because the Petrel survey data were recorded with real-time low- and high-cut filters of 8 Hz at 18 dB/octave and 62 Hz at 72 dB/octave, respectively, which limited the available bandwidth. Hence, the design of the deterministic filters was compromised by the fact that only the first streamer ghost notch lies within the recorded frequency range, so it is not possible to constrain the tow depth of the source, which is necessary for the accurate calculation of the debubble and deghost filters.

CONCLUSIONS

We have shown that deterministic filters designed from the seismic data can suppress the remnant source bubble pulse and frequency-limiting ghost notches. The strategy uses two filters. The first is a nondirectional debubble filter applied prestack that compresses the source wavelet to a band-limited spike con-

volved with the source and receiver ghosts. The second, the deghost filter, is applied poststack and suppresses the ghost notches in the power spectrum and hence expands the bandwidth and improves the geological interpretability of thick sedimentary sequences. A detailed comparison of possible processing routes show the following.

- Inverse filters based on the modeled far-field source wavelets tend to amplify high-frequency noise because the source directivity of the modeled data does not match the real data.
- Using a notional source function (source without free-surface reflection) to derive a prestack filter followed by a poststack filter designed to suppress the average source and receiver ghosts offers a simple processing strategy to obtain a high-bandwidth image. This is because the stack averages out the variability and directionality in the ghost responses.
- The prestack debubble filter designed from the seismic data was more effective than the equivalent filter derived from a modeled source at low frequencies but less effective at high frequencies close to the source and receiver notches and in the initial seismic pulse where the minimum-phase assumption used to recover the source wavelet from the real data is no longer valid. Failure of the modeled source function to adequately suppress the actual source bubble is a concern and may have implications for other processing steps.
- Either of the deterministic processing routes using a prestack debubble, designed from the data or a model, and poststack deghost filters gives an image that is better for interpretation than processing routes based on conventional statistical filters.

The conditions required for the deterministic filter processing strategy presented here are that at least part of the seismic data are from a deepwater environment (>800-ms two-way traveltime), throughout acquisition the recording streamer should be well balanced, the air-gun source volume should be stable, and any recording instrumentation low- and high-cut software filters are beyond the usable frequency range. However, we note some potential weaknesses caused mainly by short-period changes in source or streamer configuration or geometries. In theory, source dropouts can be handled as the prestack filter is applied on a shot-by-shot basis; however, changes in the ghost response cause local reverberation because the deghost filter is applied poststack. Because the CMP binning will select traces from a sequence of shots for each stacked trace, the survey will have to progress over half a spread length before it is possible to design a stable deghost filter again.

Potentially, a large volume of legacy seismic data is suitable for the strategy described in this paper. Further, the nondirectional prestack deconvolution debubble filter may be useful to precondition data for velocity analysis where the remnant bubble pulse can cause spurious semblance peaks or prior to free-surface multiple suppression.

REFERENCES

Alley, N. F., and L. A. Frakes, 2003, First known Cretaceous glaciation: Livingston Tillite Member of the Cadna-owie Formation, South Australia: Australian Journal of Earth Sciences, **50**, 139–144, doi:10.1046/j.1440-0952.2003.00984.x.

Borissova, I., 2002, Geological framework of the Naturaliste Plateau: Geoscience Australia Record, 2002/20.

Bornemann, A., R. D. Norris, O. Friedrich, B. Beckmann, S. Schouten, J. S. Sinninghe Damsté, J. Vogel, P. Hofmann, and T. Wagner, 2008, Isotopic evidence for glaciation during the Cretaceous supergreenhouse: Science, **319**, 189–192, doi:10.1126/science.1148777.

Canales, L., 1984, Random noise reduction: 54th Annual International Meeting, SEG, Expanded Abstracts, 525.

Cohen, J. K., and J. W. Stockwell Jr., 2009, CWP/SU: Seismic Un*x Release No. 41, an open source software package for seismic research and processing: Center for Wave Phenomena, Colorado School of Mines.

Davies, T. A., B. P. Luyendyk, et al., 1974, Shipboard site reports, site 258. Initial reports of the Deep Sea Drilling Project, Leg 26, *in* T. A. Davies, B. P. Luyendyk, et al., eds., Initial Reports of the Deep Sea Drilling Project, **26**, 359–414, U.S. Government Printing Office.

Direen, N. G., I. Borissova, H. M. J. Stagg, J. B. Colwell, and P. A. Symonds, 2007, Nature of the continent-ocean transition zone along the southern Australian continental margin: A comparison of the Naturaliste Plateau, SW Australia, and the central Great Australian Bight sectors, *in* G. D. Karner et al., eds., Imaging, mapping and modelling continental lithosphere extension and breakup: Geological Society Special Publication 282, 235–261.

Direen, N. G., H. M. J. Stagg, P. A. Symonds, and J. B. Colwell, 2008, Architecture of volcanic rifted margins: New insights from the Exmouth-Gascoyne margin Western Australia: Australian Journal of Earth Sciences, **55**, 341–363, doi:10.1080/08120090701769472.

Fluteau, F., G. Ramstein, J. Besse, R. Guiraud, and J. P. Masse, 2007, Impacts of palaeogeography and sea level changes on mid-Cretaceous climate: Palaeogeography, Palaeoclimatology, Palaeoecology, **247**, 357–381, doi:10.1016/j.palaeo.2006.11.016.

Ford, A. B., 1975, Volcanic rocks of Naturaliste Plateau, eastern Indian Ocean, Site 264, *in* D. E. Hayes et al., eds., Initial Reports of the Deep Sea Drilling Project, **28**, 821–833, U.S. Government Printing Office.

Gorter, J. D., and I. Deighton, 2002, Effects of igneous activity in the offshore northern Perth Basin—Evidence from petroleum exploration wells,

2D seismic and magnetic surveys, *in* Western Australian Basins Symposium III: Petroleum Exploration Society of Australia, Perth, 875–899.

Hale, D., 1984, Dip moveout by Fourier transform: Geophysics, **49**, 741–757, doi:10.1190/1.1441702.

Halpin, J. A., A. J. Crawford, N. G. Direen, M. F. Coffin, C. J. Forbes, and I. Borissova, 2008, Naturaliste Plateau, offshore Western Australia: A submarine window into Gondwana assembly and breakup: Geology, **36**, 807–810, doi:10.1130/G25059A.1.

Hardy, R. J. J., and R. W. Hobbs, 1991, Multiple suppression in deep water, *in* Continental lithosphere: Deep seismic reflections: American Geophysical Union Geodynamics Series 22, 383–390.

Hargreaves, N. D., 1992, Air-gun signature and the minimum-phase assumption: Geophysics, **57**, 263–271, doi:10.1190/1.1443239.

Hobbs, R., and H. Jakubowicz, 2000, Marine source signature measurement using a reference seismic source: 70th Annual International Meeting, SEG, Expanded Abstracts, 57–60.

Iasky, R. P., 1993, A structural study of the southern Perth Basin, Western Australia: Geological Survey of Western Australia Report 31.

Jongsma, D., and P. Petkovic, 1977, The structure of the Naturaliste Plateau and trough: APEA Journal, **17**, 3–12.

Kragh, E., J. Robertsson, R. Laws, L. Amundsen, T., Røsten, T. Davies, K. Zerouk, and A. Strudley, 2004, Rough sea deghosting using wave heights derived from low frequency pressure recordings—A case study: 65th Meeting, European Association of Geoscientists and Engineers, Expanded Abstracts, H024.

Laws, R., and E. Kragh, 2000, Time lapse seismic and the rough-sea wavelet: 70th Annual International Meeting, SEG, Expanded Abstracts, 1603–1606.

Maresh, J., R. S. White, R. W. Hobbs, and J. R. Smallwood, 2006, Seismic attenuation of Atlantic margin basalts: Observations and modeling: Geophysics, **71**, no. 6, B211–B221, doi:10.1190/1.2335875.

Mory, A. J., and R. P. Iasky, 1996, Stratigraphy and structure of the onshore northern Perth Basin, Western Australia: Geological Survey of Western Australia Report 46.

Petkovic, P., 1975, Origin of the Naturaliste Plateau: Nature, **253**, 30–33, doi:10.1038/253030a0.

Russell, B., D. Hampson, and J. Chun, 1990, Noise elimination and the Radon transform: The Leading Edge, **9**, no. 10, 18–23, doi:10.1190/1.1439677.

Sheriff, R. E., and L. P. Geldart, 1995, Exploration seismology: Cambridge University Press.

van der Baan, M., 2008, Time-varying wavelet estimation and deconvolution by kurtosis maximization: Geophysics, **73**, no. 2, V11–V18, doi:10.1190/1.2831936.

Verschuur, D. J., A. J. Berkhout, and C. P. A. Wapenaar, 1992, Adaptive surface-related multiple elimination: Geophysics, **57**, 1166–1177, doi:10.1190/1.1443330.

Yilmaz, Ö., 2001, Seismic data analysis, vol. 1: SEG.

Ziolkowski, A. M., 1984, The Delft airgun experiment: First Break, **3**, 9–18.

Ziolkowski, A. M., W. E. Lerwill, W. E. March, and L. G. Peardon, 1980, Wavelet deconvolution using the source scaling law: Geophysical Prospecting, **28**, 872–901, doi:10.1111/j.1365-2478.1980.tb01266.x.

Ziolkowski, A., G. Parkes, L. Hatton, and T. Haugland, 1982, The signature of an air-gun array: Computation from near-field measurements including interactions: Geophysics, **47**, 1413–1421, doi:10.1190/1.1441289.